Hacettepe Journal of Mathematics and Statistics
Volume 35 (2) (2006), 117 – 146

CONVECTIVE AND ABSOLUTE INSTABILITIES IN THE INCOMPRESSIBLE BOUNDARY LAYER ON A ROTATING-DISK

M. Turkyilmazoglu*

Received 02 : 01 : 2003 : Accepted 19 : 09 : 2006

Abstract

The linear absolute/convective instability mechanisms of the incompressible Von Karman's boundary layer flow over a rotating-disk are revisited in the present paper in order to review and assemble the available results in the literature on the topic. For this purpose the linearized system of stability equations of motion is first treated numerically, by employing a Spectral method based on Chebyshev collocation as well as a fourth-order Runge-Kutta method in combination with a shooting strategy. Inviscid/viscous stationary and travelling modes which lead to both convective and absolute instability mechanisms were successfully reproduced and compare favorably with those obtained by previous investigators. The validation of the zero-frequency upper-branch modes was also accomplished by the asymptotic expansion technique of [17], which is later extended to cover the non-zero frequency disturbances. The importance of the present study lies in understanding the roles of possible instability mechanisms on the laminar-turbulent transition phenomenon in the three-dimensional boundary layer flow over a rotating-disk, as well as related aerodynamic bodies.

Keywords: Rotating-Disk Flow, Absolute Versus Convective Instability, Matched Asymptotic Expansion, Laminar-Turbulent Transition.

2000 AMS Classification: 76 E 15.

*Mathematics Department, Hacettepe University, 06532 Beytepe, Ankara, Turkey.
E-mail : turkyilm@hotmail.com

1. Introduction

Many types of instability mechanism may be operational during the physical process of transition from laminar flow to turbulence in fully three dimensional boundary layer flows. In this study we deal primarily with the stability of the three dimensional boundary layer flow due to a rotating-disk. The stability properties of this flow are similar to those due to the flow over a swept-back wing in the sense that both flows are subject to inviscid crossflow vortex instability induced by the inflectional character of the mean velocity profile. The present paper will review particularly the recent progress made towards elucidating the roles of the instability mechanisms for the special case of the three-dimensional boundary layer flow due to a rotating-disk.

The concept of absolute versus convective instability has been introduced by [6] and [4] in plasma physics. A recent review of the topic relating to fluid flows can be found in [20]. Absolute/convective instability describes the behavior of the impulse response (or Green's function) to a forcing of an unstable medium. If an impulsively generated small amplitude disturbance wave grows exponentially in time at every fixed position in space, the laminar state is termed absolutely unstable. Examples of such flows are closed flow systems such as the Taylor-Couette flow and Benard convection. However, if the resulting wave packet is convected away from the source location and ultimately leaves the flow undisturbed then the flow is said to be convectively unstable. Plane-Poiseuille flow and mixing layer flow (mixing layers can also show absolute instability, see [19]) are examples of convective instability.

The early works on the stability of rotating-disk flow enlightened many of the aspects relating to the convective nature of the flow. The experimental work of [16] (hereafter referred to as GSW) clearly demonstrated the presence of co-rotating stationary vortices, which arose due to the amplification of zero-frequency waves. From the theoretical point of view, the inviscid stability properties were first investigated by GSW. Both travelling waves and stationary waves were studied. Malik [26] calculated the neutral stability curve for stationary disturbances and he additionally showed the existence of a viscous stationary mode which corresponds to zero mean wall shear stress of the crossflow velocity profile. The high Reynolds number asymptotic structure of the viscous mode of [26] was elucidated by [17]. By considering nonlinear effects and following the framework set up by [17], [25] extended Hall's asymptotic analysis and obtained an amplitude equation for the growth of disturbances close to the neutral location. The nonlinear theory showed that the instability is subcritical. [2] conducted a theoretical analysis of some aspects of linear and nonlinear non-stationary vortices in the rotating-disk flow and, in particular, investigated the properties of neutrally stable nonlinear modes. The stability curves for travelling disturbances have been computed numerically by [1].

Instead of a pure review of the literature, we intend here to validate and compare the available results by reproducing them using both numerical and analytical means. The first objective of the current work is thus to investigate numerically, the neutral/spatial/temporal stability characteristics of disturbances evolving over a rotating-disk boundary layer flow. For this reason, the linear disturbance equations are derived in a rational manner using approximations which are self-consistent. When the non-parallel terms are ignored with an additional assumption of r (the radial distance from the center of the disk) being set to 1, the traditional sixth-order stability equations are arrived at. These equations, which have been treated before by [26] and [1], are solved here using a different technique based on Chebyshev collocation with a staggered grid structure. A Runge-Kutta scheme was also employed for checking the self-consistency of our results. The use of spatio-temporal linear stability analysis shows that, in line with the literature,

three families of eigenfunctions are possible in the rotating-disk flow. Monitoring the development of the eigenvalues corresponding to these families shows branch interchanging between distinct waves at certain Reynolds numbers.

A second objective is to study the non-stationary upper branch behavior of the disturbances from an analytical point of view. For this purpose the asymptotic framework of [17] has been extended to include non-zero frequency waves. An investigation of the second-order eigenvalue problem, allowing viscous and non-stationary effects to appear, reveals the appearance of a phase shift across the critical layer and a wall layer shift. The matching of these shifts generates an eigenrelation for the non-stationary modes which is akin to the one obtained by [17] and [7] for stationary modes.

Singularities arising in the dispersion relationship enable the nature of the instability to be determined. The variation of the Reynolds number can cause such points to occur in the flow field and thus alter the behavior of a flow from a convectively unstable state to an absolutely unstable regime. These points form whenever modes associated with waves propagating in the opposite or the same directions coalesce. If the coalescing branches originate from the waves propagating in opposite directions, the singularity which causes *resonance* is said to be of pinch-type. For linearly unstable systems such a direct resonance point separates an absolutely unstable region from a convectively unstable region. Examples of flows demonstrating this phenomenon are near-wake flows ([5], [29] and [33]), swept-hiemenz flow ([32]) and mixing layer flows with backflow ([19]). On the other hand, if the two coalescing modes originate from waves propagating in the same direction, then the corresponding singularity is of the double-pole type. When these coalescing modes are nearly neutral, the damping rates are very small and thus a resulting short-term algebraic growth for small times or short distances may carry the whole system into the nonlinear stage long before the exponentially growing mode does. This is the case addressed by, amongst others, [3], [21] and [31] for Plane-Poiseuille flow and Blasius boundary layer flow. Both resonance cases were numerically examined by [8, 9] when the disk is coated by a compliant material. The secondary instability mechanism due to the absolutely unstable waves was also studied by [30].

The study of [23] has motivated us to reinvestigate the absolutely unstable viscous regime for the rotating-disk boundary layer flow and to demonstrate whether this range matches onto the absolutely unstable inviscid flow regime of [23] in the limit for high Reynolds number. Lingwood's calculations were done using only a fourth-order Runge-Kutta integrating method, but in this study we use a Spectral collocation technique. In fact, the recent asymptotic study of [18] showed that the family of branch points discovered by [23] is not the viscous continuation of the inviscid branch points, but is fundamentally of a viscous long-wave character. Our numerical results well justify the asymptotic results of [18].

The numerical simulation outcomes of [10, 11] pointed to the fact that absolute instability is not an eventually dominated mode but that the transition seems to be as a result of the convective nature of the rotating-disk boundary layer flow. There is then the possibility that nonlinearity may be first triggered by the direct spatial resonance instability mechanism. A numerical task is therefore undertaken here to search for the Reynolds numbers at which direct spatial resonance takes place. The results demonstrate that the family I and II branches both of which originate in the same wave-number plane form a direct spatial resonance at a Reynolds number of about 445, at which the flow is still laminar.

This review consists of two interrelated parts organized as follows. The first part is devoted to convective instability and the second part to absolute and direct spatial resonance instabilities. In §2 the general governing equations of the motion are given followed

by the linear stability theory in §3-4. The linear stability results are then presented in §5-5.5. For the second part, in §6 a definition of absolute/convective instabilities based on Briggs pinching criterion is presented and also the absolute instability results are given in §7. §8 involves the modal coalescence results. Further discussion and conclusions follow in §9.

2. The basic equations

2.1. Governing equations of the flow. We consider the three dimensional boundary layer flow of an incompressible fluid on an infinite disk which rotates about its axis with a constant angular velocity Ω. The Navier-Stokes equations are non-dimensionalized with respect to a lengthscale $L = r_e^*$, velocity scale $U_c = L\Omega$, timescale L/U_c and pressure scale ρU_c^2, where ρ is the fluid density. This leads to a global Reynolds number $Re = \frac{U_c L}{\nu} = R^2$, where R is the Reynolds number based on the displacement thickness $\delta = (\frac{\nu}{\Omega})^{\frac{1}{2}}$. Thus, relative to non-dimensional cylindrical polar coordinates (r, θ, z) which rotate with the disk, the full time-dependent, unsteady Navier-Stokes equations governing the viscous fluid flow are the usual momentum and the continuity equations, and these are given as follows:

$$
\begin{aligned}
&\frac{\partial u}{\partial t} + u\frac{\partial u}{\partial r} + \frac{v}{r}\frac{\partial u}{\partial \theta} + w\frac{\partial u}{\partial z} - \frac{v^2}{r} - 2v - r = -\frac{\partial p}{\partial r} + \frac{1}{R^2}[\nabla^2 u - \frac{2}{r^2}\frac{\partial v}{\partial \theta} - \frac{u}{r^2}],\\
&\frac{\partial v}{\partial t} + u\frac{\partial v}{\partial r} + \frac{v}{r}\frac{\partial v}{\partial \theta} + w\frac{\partial v}{\partial z} + \frac{uv}{r} + 2u = -\frac{1}{r}\frac{\partial p}{\partial \theta} + \frac{1}{R^2}[\nabla^2 v + \frac{2}{r^2}\frac{\partial u}{\partial \theta} - \frac{v}{r^2}],\\
&\frac{\partial w}{\partial t} + u\frac{\partial w}{\partial r} + \frac{v}{r}\frac{\partial w}{\partial \theta} + w\frac{\partial w}{\partial z} = -\frac{\partial p}{\partial z} + \frac{1}{R^2}[\nabla^2 w],\\
&\frac{\partial u}{\partial r} + \frac{1}{r}\frac{\partial v}{\partial \theta} + \frac{\partial w}{\partial z} + \frac{u}{r} = 0.
\end{aligned} \tag{1}
$$

The Laplacian operator in cylindrical coordinates is given as

$$
\nabla^2 = \left(\frac{\partial^2}{\partial r^2} + \frac{1}{r^2}\frac{\partial^2}{\partial \theta^2} + \frac{\partial^2}{\partial z^2} + \frac{1}{r}\frac{\partial}{\partial r}\right). \tag{2}
$$

In this analysis the fluid is assumed to lie in the semi-infinite space $z \geq 0$. In the above equations the curvature effects as well as the effects stemming from the Coriolis forces are present. It is now well known that these terms have a strongly stabilizing impact in the linear stability theory, as pointed out by [27] and [34].

2.2. The mean flow. The dimensionless mean-flow velocities and pressure are given by Von Kármán's exact self-similar solution of the Navier-Stokes equations for steady laminar flow. The boundary layer coordinate Z, which is of order O(1) is defined as $Z = zR$, and the self-similar equations take the form

$$
(u_B, v_B, w_B, p_B) = (rF[Z], rG[Z], \frac{1}{R}H[Z], \frac{1}{R^2}P[Z]), \tag{3}
$$

where the functions F, G, H and P satisfy the following ordinary differential equations

$$
\begin{aligned}
&F^2 - (G+1)^2 + F'H - F'' = 0,\\
&2F(G+1) + G'H - G'' = 0,\\
&P' + H'H - H'' = 0,\\
&2F + H' = 0.
\end{aligned} \tag{4}
$$

Here primes denote derivative with respect to Z and the appropriate boundary conditions are given as

$$\begin{aligned} &F = G = H = 0 \text{ at } Z = 0, \\ &F = 0,\ G = -1,\ H = h_\infty \text{ as } Z \to \infty. \end{aligned} \tag{5}$$

The value of h_∞ is a constant vertical velocity of the rotating fluid in the far-field above the disk, and it has to be found numerically in the course of the solution of equations (4) and (5).

3. Derivation of the linear stability equations

3.1. Viscous disturbance equations. We are here interested in perturbation solutions of Von Kármán's self-similarity velocity profiles (3). The instantaneous non-dimensionalized velocity components imposed on the basic steady flow are u, v, w and the pressure component p, and they can be expressed as

$$u[r, \theta, z, t] = u_B + u'[r, \theta, z, t].$$

Having linearized the equations for small perturbations, we find that the linearized Navier-Stokes operator has coefficients independent of θ and hence the disturbances can be decomposed into a normal mode form proportional to $e^{iR(\beta\theta - \omega t)}$. Such an approximation leads the disturbances to be wave-like, separable in θ and t. Consequently, the perturbations may be assumed to be of the form

$$u' = \tilde{f}[r, Z] e^{[iR(\beta\theta - \omega t)]} + c.c.,$$

where β and ω are respectively the wave-number in the azimuthal direction and the scaled frequency of the wave propagating in the disturbance wave direction.

The separation in θ and t simplifies the linear system of equations. However no such simplification arises as far as the r dependence is concerned (except in the limit as $R \to \infty$) and the full linearized partial differential system has to be solved subject to suitable initial conditions to determine the stability of the flow. Consider next the limit $R \to \infty$ and introduce the scale $X = Rr$ which is the appropriate scale on which the disturbances develop. After allowing for the multiple-scale replacement of $\frac{\partial}{\partial r}$ by

$$R\frac{\partial}{\partial X} + \frac{\partial}{\partial r},$$

and keeping only terms of $\mathrm{O}(1/R)$, the reduced system of equations stemming from these approximations can be written in the following form

$$\begin{aligned} &f'' - Hf' - [iR(\alpha F + \beta G - \bar{\omega}) + \lambda^2 + F]f + 2(G+1)g - RF'h - i\alpha Rp = 0, \\ &g'' - Hg' - [iR(\alpha F + \beta G - \bar{\omega}) + \lambda^2 + F]g - 2(G+1)f - RG'h - i\beta Rp = 0, \\ &h'' - Hh' - [iR(\alpha F + \beta G - \bar{\omega}) + \lambda^2 + H']h - R\tilde{p}' = 0, \\ &\bar{\alpha} f + i\beta g + h_z = 0, \end{aligned} \tag{6}$$

where $\lambda^2 = \alpha^2 + \beta^2$, $\bar{\alpha} = i\alpha + \frac{1}{R}$. It should be pointed out that the non-parallel terms which are of $\mathrm{O}(1/R)$ were also dropped from equations (6). The linear equation system above is identical to the one used by previous investigators, see for instance [26] and [23].

The boundary conditions for this set of equations are $f = g = h = 0$ at the solid wall ($Z = 0$). Considering the decaying property of the disturbances, the boundary conditions to be imposed far away from the disk surface are derived from the asymptotic form of equations (6).

3.2. Inviscid Rayleigh equation. Further neglect of all the terms of order R^{-1} in (6) leads to the well-known Rayleigh equation

$$[(\alpha F+\beta G-\omega)(D^2-\lambda^2)-(\alpha D^2F+\beta D^2G)]h=0, \tag{7}$$

where, $\lambda^2=\alpha^2+\beta^2$ and $D=\frac{\partial}{\partial Z}$.

4. Solution Technique

4.1. Spectral treatment of the stability equations. The discretization technique we use here is a Spectral collocation method using Chebyshev polynomials as basis functions. A staggered grid is used only in the Z direction. The pressure is defined at the cell centers, at half points, but other components at the cell faces. Since no pressure points fall on the boundary, the critical boundary conditions for the pressure have therefore been avoided. Momentum equations are thus collocated at Gauss-Lobatto points $\cos[k\frac{\pi}{N}]$, whereas the continuity equation is imposed at Gauss points $\cos[(k+\frac{1}{2})\frac{\pi}{N}]$. The Chebyshev interpolation between these two different grids, from cell centers to cell faces or otherwise is then employed as given in [28].

The computational physical plane has been mapped onto the Spectral space by means of the linear transformation

$$\eta=-1+\frac{2}{Z_{max}}Z. \tag{8}$$

Here Z_{max} is the far-field boundary of the flow, which throughout the calculations is set to a finite value of 20, about 4 times the boundary layer thickness.

The resulting equations from the discretization ultimately can be assembled as a large generalized matrix-eigenvalue problem of the form

$$LU=0, \tag{9}$$

where L is a $(4N+3)\times(4N+3)$ full matrix and $U=[f,g,h,p]^T$ is the eigenfunction. The incorporation of boundary conditions only necessitates some modifications to the first and last row of the matrix L.

4.2. Newton-Raphson searching technique for the branch points. To determine a branch point in the ω and α complex planes, we have to fix β and R, and shoot for simultaneous zeros of both the dispersion relation and the group velocity $\frac{\partial\omega}{\partial\alpha}$. The corrections to α and ω which are denoted by $\delta\alpha$ and $\delta\omega$ (which are complex in general) can be obtained from the solution of the following linear equations

$$\begin{aligned} U^1(\eta=-1)+\delta\alpha\frac{\partial U^1}{\partial\alpha}(\eta=-1)+\delta\omega\frac{\partial U^1}{\partial\omega}(\eta=-1)=0,\\ \frac{\partial\omega}{\partial\alpha}+\delta\alpha\frac{\partial^2\omega}{\partial\alpha^2}+\delta\omega\frac{\partial^2\omega}{\partial\alpha\partial\omega}=0. \end{aligned} \tag{10}$$

Note that the variables are complex-valued, therefore they can be written in the matrix form

$$J\Delta=-\mathrm{RHS}, \tag{11}$$

where, J is a full 4×4 square matrix of coefficients, RHS is a 4×1 known vector and $\Delta=[\delta\alpha,\delta\omega]^T$.

In computing the neutral branch points one has to consider the following equations

$$\begin{aligned} \left[U^1+\delta\alpha\frac{\partial U^1}{\partial\alpha}+\delta\omega\frac{\partial U^1}{\partial\omega}+\delta R\frac{\partial U^1}{\partial R}\right]_{\eta=-1}=0,\\ \frac{\partial\omega}{\partial\alpha}+\delta\alpha\frac{\partial^2\omega}{\partial\alpha^2}+\delta\omega\frac{\partial^2\omega}{\partial\alpha\partial\omega}+\delta R\frac{\partial^2\omega}{\partial\alpha\partial R}=0. \end{aligned} \tag{12}$$

Here, we fix the azimuthal wave-number β as real and the increment $\delta\omega$ is now also real. After one solution of the matrix equation (9) the quantity $U^1(\eta = -1)$ is now known. The corresponding group velocity can be calculated by two different approaches itemized as follows

(i) Solve the matrix equation at successive α_0, $\alpha_0 - \delta\alpha$ and $\alpha_0 + \delta\alpha$. Then, store the corresponding frequencies as ω_0, ω_{-1} and ω_1. This set of eigenvalues is then used to approximate the group velocity $\frac{\partial\omega}{\partial\alpha}$ as $\frac{\omega_1-\omega_{-1}}{2\delta\alpha}$ and the second derivative of the group velocity $\frac{\partial^2\omega}{\partial\alpha^2}$ as $\frac{\omega_1-2\omega_0+\omega_{-1}}{\delta\alpha^2}$. To compute successive derivatives of the group velocity and the derivatives of the eigenfunctions required in the equations (10) and (12), we can simply use the same procedure.

(ii) From the Taylor expansion we can approximate the group velocity as

$$\frac{\partial\omega}{\partial\alpha} = -\frac{\frac{\partial U^1}{\partial\alpha}}{\frac{\partial U^1}{\partial\omega}}(\eta = -1). \tag{13}$$

However, one can estimate the derivatives of the eigenfunctions with respect to α and ω by differentiating (9) to give

$$\begin{aligned} L\frac{\partial U}{\partial\alpha} &= -\frac{\partial L}{\partial\alpha}U, \\ L\frac{\partial U}{\partial\omega} &= -\frac{\partial L}{\partial\omega}U. \end{aligned} \tag{14}$$

Having solved the matrix equation (11), the corrections Δ are added to the previous eigenvalues to give a better approximation and reduce the discrepancies on the wall boundary condition. Then, an iterative scheme is employed until the magnitude of $U^1(\eta = -1)$ and $\frac{\partial\omega}{\partial\alpha}$ are simultaneously less than some small prescribed value.

5. Linear stability results

5.1. Basic velocity profiles. In the solution procedure, the equations (4) were reduced to a system of first order differential equations and then solved by a fourth-order Runge-Kutta scheme combined with a shooting procedure. The far-field boundary condition $Z_{max} = 20$ was found to be satisfactory and the corresponding normal velocity h_∞ was then calculated up to 6 digits as 0.884423 from this method. The computed velocity distribution for the basic flow on the rotating-disk is shown in Figure 1 (a). This similarity solution has been used by the researchers cited herein, see for instance [23] and [15]. A combination of the radial and azimuthal velocities leads to a profile which is inflectional and which contributes to the occurrence of crossflow instability in the rotating-disk flow. A few examples of these profiles are shown schematically in Figure 1 (b) at several Reynolds number locations, for both stationary ($\omega = 0$) and a non-stationary ($\omega = 7.9$) case.

From the literature, two types of instability waves are known to exist in the rotating-disk boundary layer flow that cause either convective or absolute instabilities. The first one is the inviscid-type or the upper branch and the other one is the viscous-type or the lower branch. We will investigate these two distinct branches in more detail in the following sections.

5.2. Neutral waves.

5.2.1. *Stationary and travelling waves.* Neutral curves play a key role in the determination of the bounds of the stability. For comparison purposes, the neutral curves for both stationary and non-stationary waves in the (R, α) and (R, ε) planes are shown in

Figures 1 (c-d) for a negative and several positive non-dimensional frequencies. The wave-angle ε of a disturbance is defined as $\varepsilon = \arctan[\frac{\beta}{\alpha_r}]$. These curves are very similar to the ones calculated previously by [26] and also [1]. In line with the findings of the latter, it is noticed that a minimum occurs on the lower branch for certain fixed frequencies. The existence of such second minima was also observed in the experiments of [12] and [13].

For the negative frequency $\omega = -5.0$ in Figure 1 (c), there are no longer two minima. Compared to zero-frequency disturbances, instability starts much earlier at a smaller critical Reynolds number. The corresponding critical Reynolds number for a negative frequency of $\omega = -5.0$ is $R = 284.910$ and the associated eigenvalues are $\alpha = 0.36310$, $\beta = 0.10710$ and $\varepsilon = 16.46^\circ$, respectively. At $\omega = 4.0$ the critical Reynolds number and the eigenvalues in Figure 1 (c) are $R = 297.630$, $\alpha = 0.40302$, $\beta = 0.05601$ and $\varepsilon = 7.96^\circ$ for the upper branch and $R = 172.820$, $\alpha = 0.15210$, $\beta = 0.01202$ and $\varepsilon = 4.48^\circ$ for the lower branch, respectively. The same values for $\omega = 10.0$ are $R = 329.371$, $\alpha = 0.43001$, $\beta = 0.03203$ and $\varepsilon = 4.20^\circ$ for the upper branch and $R = 68.709$, $\alpha = 0.33601$, $\beta = -0.12903$ and $\varepsilon = -20.98^o$ for the lower branch, respectively. And finally, the lowest critical Reynolds number for the lower branch occurs at frequency $\omega = 7.9$. The corresponding eigenvalues are $R = 64.443$, $\alpha = 0.27597$, $\beta = -0.10669$ and $\varepsilon = -20.87^o$, respectively. When the frequency increases beyond 7.9 the lower critical Reynolds number starts increasing too. The aforementioned critical values are almost indistinguishable from those obtained by [1].

The wave-angle stability curves are depicted in Figure 1 (d). On the upper branch the non-zero frequency waves approach the zero-frequency neutral curve at large Reynolds numbers. Increasing frequency causes loops on the upper branch. However, these do not correspond to a bifurcation. The resulting intersections of the curves is an artifact of projecting the curves onto the plane. We can conclude that there exist a critical angle below which all the waves are linearly damped. This critical angle is, according to our calculations, -35.34° at a frequency 7.9. The same angle at frequency 10 is -35.04°. This angle is given in [1] as -50.4°. From a consideration of the Rayleigh equation, for positive frequencies we have found that basic velocity profiles cease to have a point of inflexion for values of $\varepsilon < -36.9^\circ$, and therefore there are no unstable eigenvalues for angles less than this critical value. This value is consistent with our numerical computations cited above for large Reynolds numbers. The wave-angle continuously increases on the lower branch for increasing Reynolds numbers. It is known that the direction of zero wall mean shear stress corresponds to a critical angle of about 39.64°, see [17]. At $R = 10^6$ the corresponding wave-angle was found to be 39.216°.

5.3. Spatial and temporal waves. In this section we examine the spatial/temporal instability characteristics of Von Kármán's basic velocity profile as shown in Figure 1. The spatial amplification rate $(-\alpha_i)$ contours are drawn for certain frequencies. Figure 2 (a-c) show these contours in the (R, α), (R, β) and (R, ε) planes for the stationary waves, and Figures 2 (d-f) show the results for frequencies $\omega = 4$. In good agreement with the results of [1], all these contours show a linear variation as the growth rate increases in magnitude. Beyond some critical amplification rate the second minimum disappears for a fixed frequency. From the stationary stability diagram Figure 2 (c) it can be seen that the most unstable wave-angle varies slowly with Reynolds number on the upper branch.

We have also plotted the growth rate curves at some selected Reynolds numbers. Figure 3 shows the spatial growth rate $(-\alpha_i)$ curves at $R = 1000$ as a function of wave-angle. On the lower branch the growing waves originate almost from the same place at a wave-angle of about 11.45^o, on the other hand, the upper branch amplifying waves originate at a larger wave-angle as R increases. Travelling waves with a frequency of 10

are shown in Figure 3 (b). This graph suggests that travelling waves are less amplified than the stationary ones. It should be remarked that as will be shown later the flow is already absolutely unstable at $R = 1000$ and a true spatial growth rate for time-periodic disturbances is unlikely to occur physically. Figures 3 (a-b) are thus shown only for mathematical interest and comparison purposes. In Figures 3 (c-d), spatial calculations are shown to determine the frequency of the most unstable wave of family 1 (see below) modes at $R = 500$. It can be seen from Figure 3 (c) that unlike the stationary waves the travelling waves are the most unstable. Moreover, the most unstable region is dominated by the negative frequency region with the phase velocity $\frac{\omega}{\sqrt{\alpha_r^2+\beta^2}}$ directed inwards.

Next, the evolution of different families of eigenfunctions is considered. The spatial families of the stationary eigen-solutions originating at $R = 400$ are shown in Figures 4 (a-f). As shown, the family 1 branches have neutral points on the upper and lower branches of the neutral curve. Unlike the family 2, which includes only downstream propagating damped waves, family 1 involves both damped and amplified downstream propagating waves in a specific range of wave-numbers. The third family which seems to be only on the lower α plane has no neutral points at all and is characterized by large values of $-\alpha_i$, corresponding to upstream propagating damped waves.

The behavior of the stationary eigenfamilies has also been captured in the work of [1]. A similar trend of non-stationary disturbances at $\omega = 7.9$ is shown in Figures 4 (d-f), at a Reynolds number of 400. The main difference is that family 2 in this case also has a neutral branch point at $R = 400$. This is a result of lower branch instability for the positive frequencies. It should also be mentioned that we have investigated the real part of the group velocity given by $\frac{\partial\omega}{\partial\alpha}$. We found that for the most part, for family 3 up to $\beta = 0.04$, the real part remains negative, and the real part of the group velocity angle is less than -90^o. This indicates an inward energy transfer towards the center of the disk. Consequently, the waves in this direction are strongly damped. However, for β less than 0.04 the group velocity vector is directed outward and so the waves are amplified in this direction.

Figures 3-4 point to another mechanism for instability. In particular, branch switching in spatial stability calculations can be effectively used as an indication of qualitative change in the nature of the instability from convective to absolute or vice versa. We shall investigate this feature of the rotating-disk flow further in a later section.

5.4. Contour lines and cross-flow vortices. In this part, we display contour plots and vector fields with cross-flow vortices for the frequencies $\omega = 0$ and $\omega = 7.9$ in Figures 5 and 6. The contours contain the velocity components

$$\alpha F + \beta G + Re[(\alpha f + \beta g)e^{[(i\alpha r+\beta R\theta-\omega t)]}], \tag{15}$$

$$\frac{H}{R} + Re[(h)e^{[(i\alpha r+\beta R\theta-\omega t)]}] \tag{16}$$

for various Reynolds numbers. In each figure the portions (a) and (c) refer to (15) and portions (b) and (d) refer to (16). "Cat's eye" patterns, which are a characteristic feature of the cross-flow instability, are clearly seen in these contour diagrams.

Vector plots are shown in Figures 6 (a-b) for the stationary cross-flow vortices and Figures 6 (c-d) for the travelling waves. There are essentially two sets of vortices present. The first set of vortices are nearest to the wall as suggested by Stuart in GSW. Furthermore, they have formed only on the upper branches. The second set of vortex structures are more visible on the upper branches of the neutral curves. Malik [26] also displayed zero-frequency cross-flow vortices, but from his computations the near wall vortices were

not captured. As one travels from the upper branch to the lower one, the location of the vortex center also travels towards the wall.

5.5. Asymptotic analysis of the upper branch non-stationary modes. Hall [17] computed the evolution of the upper branch modes considering only the zero-frequency waves. In this section our intention is to extend his theory to include the cases where non-zero frequency waves also exist. Following the work of [17] we define a small parameter $\epsilon = R^{-1/6}$. On the upper branch we assume that the disturbances take the form

$$(U, V, W, P) = (u(z), v(z), w(z), p(z)) e^{\frac{i}{\epsilon^3}(\int^r \alpha dr + \theta\beta)} e^{-\frac{i}{\epsilon^2}\omega t},$$

and we also expand the wave-numbers and frequency as

$$(\alpha, \beta, \omega) = (\alpha_0, \beta_0, \omega_0) + \epsilon(\alpha_1, \beta_1, \omega_1) + \cdots .$$

As in the study [17], we restrict our attention to neutral disturbances at a local position r. In the following the regions where such waves develop are considered, and asymptotic solutions are sought in each region. The analysis below also follows closely the work of Cole [7].

5.5.1. *Inviscid region* $\zeta = z\epsilon^{-3}$ $(z = \mathrm{O}(R^{-1/2}))$. The existence of this inviscid zone of depth $\mathrm{O}(\epsilon^3)$ was shown by GSW. In this region u, v, w and p are expanded in the form

$$(u, v, w, p) = (u_0, v_0, w_0, p_0)(\zeta) + \epsilon(u_1, v_1, w_1, p_1)(\zeta) + \cdots ,$$

Substituting these into Equations (1), and equating the terms of order of $\mathrm{O}(\epsilon^{-3})$, the leading-order approximation leads to the inviscid Rayleigh equation, see [17]. Defining the effective velocity profile $\bar{U}_B = \alpha_0 r F + \beta_0 G$ and leading-order wave-number $\gamma_0^2 = \alpha_0^2 + \frac{\beta_0^2}{r^2}$, the solution is restricted to satisfy $\bar{U}_B$ & $\bar{U}_B''$ to vanish at a non zero $\zeta = \bar{\zeta}$, so that the singularity in the Rayleigh equation is avoided. The eigenvalue problem was solved by [17], and it was found that the unknowns α_0, β_0, γ_0 and $\bar{\zeta}$ satisfy

$$\gamma_0 = 1.16, \quad \frac{\alpha_0 r}{\beta_0} = 4.26, \quad \alpha_0 = 1.1293, \quad \frac{\beta_0}{r} = 0.2651, \quad \bar{\zeta} = 1.46. \tag{17}$$

Proceeding to the next-order in the inviscid zone, the second-order equations come from $\mathrm{O}(\epsilon^{-2})$ terms and eliminating u_1, v_1 and p_1 we obtain the non-homogeneous Rayleigh equation for w_1 in the form

$$\bar{U}_B\left[w_1'' - \gamma_0^2 w_1\right] - \bar{U}_B'' w_1 = 2\bar{U}_B \hat{\alpha} w_0 + \beta_0 r \hat{\epsilon}\left[F'' - F\frac{\bar{U}_B''}{\bar{U}_B}\right] w_0 + \omega_0 \frac{\bar{U}_B''}{\bar{U}_B} w_0, \tag{18}$$

where $\hat{\alpha} = \alpha_0\alpha_1 + \frac{\beta_0\beta_1}{r^2}$ and $\hat{\epsilon} = \frac{\alpha_1}{\beta_0} - \alpha_0\beta_1\beta_0^2$. Due to the second term on the right-hand side of (18), a Frobenius expansion reveals that a logarithmic singularity appears belonging to w_1 at $\zeta = \bar{\zeta}$. This singularity manifests itself in the form

$$w_1'' \sim \frac{k_c}{\zeta - \bar{\zeta}} w_0(\bar{\zeta}), \quad \zeta > \bar{\zeta}, \tag{19}$$

where k_c is given in Appendix A. The singularity (19) can be removed by introducing a critical layer at $\zeta = \bar{\zeta}$, and then the solution of (18) that satisfies $w_1(\infty) \to 0$ is as given in [17], except that an extra integral appears due to the non-zero frequency term in equation (18).

Taking into consideration the viscous critical layer theory, if the path of the integration is deformed into the complex plane near $\zeta = \bar{\zeta}$ (i.e, continuation below the critical layer), the following holds:

$$w_1 \sim k_c(\zeta - \bar{\zeta})\left[ln(\zeta - \bar{\zeta}) - i\,\mathrm{sgn}(\bar{U}_B'|_{\zeta=\bar{\zeta}})\pi\right] w_0(\bar{\zeta}),\ \zeta < \bar{\zeta}.$$

This and (19) give the well-known linear phase jump in the inviscid zone

$$w_1'|_{\bar\zeta_-}^{\bar\zeta_+} = i\,\mathrm{sgn}(\bar U_B'(\bar\zeta))\pi k_c w_0(\bar\zeta). \tag{20}$$

5.5.2. *Viscous sublayer* $\xi = z\epsilon^{-4}$ ($z = \mathrm{O}(R^{-2/3})$). From the leading-order equations in the inviscid zone we find that

$$\zeta \to 0, \quad i(\alpha_0 u_0 + \frac{\beta_0}{r} v_0) \to -w_0'(0).$$

Therefore, to satisfy the zero-velocity requirement at the wall, a viscous sublayer is required. Balancing the convection and diffusion terms in the disturbance equations (1), it is found that the thickness of this layer should be $\mathrm{O}(\epsilon^4)$. The basic velocity profiles are expanded as in [17]. The various quantities also expand as follows:

$$(u, v, w, p) = (\tilde u_0, \tilde v_0, 0, 0)(\xi) + \epsilon(\tilde u_1, \tilde v_1, \tilde w_0, \tilde p_0)(\xi) + \epsilon^2(\tilde u_2, \tilde v_2, \tilde w_1, \tilde p_1)(\xi) + \cdots .$$

Substituting these into the Navier-Stokes Equations (1), and after some manipulations as in [17], we find the wall layer shift for large ξ to be

$$\tilde w_0 \sim w_0'(0)\left[\xi + \frac{A_i(\xi_0)}{\lambda_0\kappa}\right],$$

with $\xi_0 = -i\frac{\omega_0}{\lambda_0^2}$, $\lambda_0^3 = i[\alpha_0 r F_0 + \beta_0 G_0]$ and $\kappa = \int_{\xi_0}^{\infty} A_i(\tau)d\tau$. On matching with the inviscid zone described earlier, we find that w_1 must satisfy

$$w_1 \to w_0'(0)\frac{A_i'(\xi_0)}{\lambda_0\kappa}, \quad \zeta \to 0. \tag{21}$$

We see from (18) that w_1 satisfies equations identical to w_0 apart from a non-homogeneous part on the right-hand side. Therefore a certain solvability condition is required to ensure that a solution exists. To proceed further this solvability condition can be obtained by multiplying (18) with w_0 and integrating from wall to infinity so that

$$\oint_0^{\infty} \frac{w_0 L w_1}{\bar U_B} d\zeta = w_0'(0)^2 \frac{A_i'(\xi_0)}{\lambda_0\kappa} - i\pi\mathrm{sgn}[\bar U_B'(\bar\zeta)] w_0^2(\bar\zeta) k_c, \tag{22}$$

where, $\oint$ denotes the finite part of the integral, $L = \frac{d^2}{dZ^2} - \gamma_0^2 - \frac{\bar U_B''}{\bar U_B}$ and the use of equations (17), (18), (20) and (21) is made. Furthermore, using equations (18) and (22) we obtain the eigen-relation

$$2\hat\alpha I_1 + r\hat\epsilon[I_2 + a] + \omega_0[I_3 + b] = w_0'(0)^2 \frac{A_i'(\xi_0)}{\lambda_0\kappa}, \tag{23}$$

where I_1, I_2, I_3, a and b are given in Appendix A.

Now using the Reynolds number Re based on the boundary layer thickness and the local azimuthal velocity of the disk, $Re = rR^{1/2}$, the effective wave-number $(\alpha^2 + \frac{\beta^2}{r^2})^{\frac12}$ and the wave-angle ε in powers of Re are given by

$$\begin{aligned} \gamma &= (\alpha^2 + \frac{\beta^2}{r^2})^{\frac12} = \gamma_0 + \frac{\hat\alpha}{\gamma_0} Re^{-\frac13} + \cdots , \\ (\tan\varepsilon)^{-1} &= \frac{\alpha_0 r}{\beta_0} + \hat\epsilon Re^{-\frac13} + \cdots . \end{aligned} \tag{24}$$

Note that if $\omega_0 = 0$ the explicit expressions for the effective wave-number and the wave-angle outlined in [17] are recovered from the eigen-relation (23). The extra term I_3 is due to our consideration of non-zero frequency waves. In this case, for any non-zero ω_0, the equation (23) should be solved numerically, to determine the wave-number correction $\hat\alpha$ and the wave-angle correction $\hat\epsilon$ in (24).

Based on these asymptotic findings, comparisons with the numerical calculations are shown in Figure 7 for $\omega = -5$, 0 and 10. In this figure the long curves show numerical

results and shorter lines asymptotic ones. Notice that to make comparisons with the numerics, ω_0 should be re-scaled by Re. It is seen that there is satisfactory agreement between the asymptotic predictions and the numerical results. In order to increase the agreement domain of numerical and asymptotic analysis for smaller Reynolds numbers, more terms of the expansions in (24) need to be calculated, but this is beyond the scope of the present study. Moreover, it is also possible to consider ω_0 as complex to further investigate temporally growing waves. Furthermore, using the asymptotic relation of the Airy function as $|\omega_0| \to \infty$, the right-hand side of (23) can be replaced by $\frac{iw_0'(0)^2\omega_0}{\lambda_0^3}$, which then gives explicit expressions for the wave-number and wave-angle corrections.

6. The absolute/convective instability of the rotating-disk flow

In this section we shall give a description of absolute/convective instabilities and further investigate under what circumstances the three dimensional boundary layer flow becomes absolutely/convectively unstable. In doing so, we shall use the ideas of [6] and [4]. The specific example we consider is the three dimensional rotating-disk boundary layer flow.

The complex dispersion relation which can be obtained through the application of classical linear stability theory to a three dimensional parallel flow can be represented in the form

$$\mathbf{D}(\alpha, \omega; \beta, R) = 0. \tag{25}$$

Note that in three dimensional flows the relation (25) defines the local instability characteristics due to the fact that parallel flow assumptions or local mean velocities have been employed.

From now on we assume that the zero normal velocity condition on the wall is replaced by a line forcing given in the form

$$\delta(r - r_f)\delta(t - t_f)e^{i\beta R\theta}, \tag{26}$$

where $\delta(r - r_f)$ and $\delta(t - t_f)$ are the Dirac delta functions at a non-dimensional radius r_f, and at a specific time t_f (=0 formally), respectively. Based on the dispersion relation (25) we can now form the impulse response or Green's function $\mathbf{G}(r, \theta, t; \beta, R)$ to the point forcing (26) associated with the operator $\mathbf{D}(-i\frac{\partial}{\partial r}, \theta, i\frac{\partial}{\partial t}; \beta, R)$ as a double integral

$$\mathbf{G}(r, \theta, t; \beta, R) = \frac{1}{4\pi^2} e^{i\beta R\theta} \int_F \int_L \hat{G} \frac{e^{i(\alpha r - \omega t)}}{\mathbf{D}(\alpha, \omega; \beta, R)} d\omega d\alpha. \tag{27}$$

The impulse response $\mathbf{G}$ above is defined as the instability wave field generated by a Dirac delta function in space and time, as posed by (26). A function $\hat{G}$ in equation (27) appears and is dependent on the normal coordinate, which essentially is the eigensolution of the governing equations (6). Although the singularities caused by $\hat{G}$ (generally the branch cuts causing the continuous singularities) are important in the inversion integrals in (27), we assume that the main contribution to the response (27) comes from the zeros of $\mathbf{D}$, which are the discrete eigenvalues obtained from (25). These eigenvalues provide a mapping between the α and ω planes defined by the F and L contours, respectively.

A rigorous mathematical criterion given by [4] and [6] can be applied to the dispersion relation (25) to determine the nature of the instability. To do that, it is necessary to perform a spatio-temporal stability analysis. The first task is to compute analytically or numerically the singularities ω_0 lying in the complex ω plane. Then the pairs of eigenvalues which contribute to a zero group velocity, i.e, $\frac{\partial \omega}{\partial \alpha}(\alpha_0) = 0$, at the corresponding complex wave-number $\alpha = \alpha_0$ are identified. Note that this wave-number is associated with the ray $\frac{r}{t} = 0$. Next, the amplification rate (also called the absolute growth rate)

at this point is given by $\omega_i = Im(\omega_0)$, which characterizes the temporal evolution of the disturbances. Finally, the criterion for the absolute or convective instability for any given flow, as outlined by [6] and [4], simply takes the form

$$\begin{aligned} &\mathrm{Im}(\omega_0) > 0 \implies \text{Absolute instability,} \\ &\mathrm{Im}(\omega_0) < 0 \implies \text{Convective instability.} \end{aligned} \tag{28}$$

Later, Briggs and Bers showed that the absolute/convective instability criterion given above is not precise enough. What should be further taken into account is that the two spatial branches associated with the second-order algebraic branch point ω_0 must lie entirely in the upper and lower half α planes, when the frequency contour L is located above all the singularities of the dispersion relation (25). The method of continuation is then used to deflect the original L contour, shown in Figure 9 (a), to the L' contour shown in Figure 9 (c). The ultimate purpose of this action is to lower the contour just below the real ω-axis (to avoid absolute growth, of course). As the contour L in the ω plane is lowered to L', the corresponding α branches in the α plane will start moving upwards/downwards. Therefore in order not to violate causality, the F contour in the α plane shown in Figure 9 (b) should also be deformed off the real α-axis into F'. Of course, the simultaneous deformation of the contours L and F into L'' and F'' (see Figures 9 (e-f)) must terminate when L'' touches $\omega(\alpha)$ and F'' becomes pinched between the two spatial branches. When α spatial branches pinch in the α plane they constitute a saddle point α_s and the mapping of F'' pinches the ω curves in the ω plane constituting a pinching frequency ω_p. Pinching occurs precisely at the point (α_s, ω_p), where the group velocity $\frac{\partial \omega}{\partial \alpha}(\alpha_s, \omega_p)$ is zero. Correspondingly a cusp appears at ω_p in the locus of $\omega(\alpha)$, a feature that can be used to detect the branch point, as demonstrated by [22]. In fact the α inversion in (27) can be made by enclosing the F'' contour with semi-circles and employing the residue theorem, assuming only the first-order poles (higher-order residues would be obtained by a limiting process of coalescing first-order poles). A subsequent integration in the ω plane leads to the following time-asymptotic response

$$\mathbf{G} \sim \frac{e^{i[\alpha_s(r-r_f)+\beta R\theta-\omega_p R(t-t_f)]}}{\left[2\pi i t \frac{\partial \mathbf{D}}{\partial \omega}\frac{\partial^2 \mathbf{D}}{\partial \alpha^2}\right]^{1/2}_{\alpha_s,\omega_p}}. \tag{29}$$

We should also bear in mind that there might be cases where the two spatial branches in the α plane of a branch point ω_p may be located, for high enough $\mathrm{Im}(\omega)$, in the same half α plane. Such pairs (α_s, ω_p) do not satisfy the so called pinching criterion, and as will be discussed later, they cause only an algebraic growth, not an absolute growth rate.

7. Absolute instability results

Our procedure for computing branch points was first verified by reproducing the results of [19] for the mixing layer problem, see Figure 8. The results shown here were obtained by solving the inviscid Rayleigh equation for the normal mode given by Equation (7), as well as the viscous sixth-order system of equations of order given by Equations (6). In this section we present these results separately and later show that the high-Reynold's number viscous modes match onto the inviscid Rayleigh modes.

7.1. Inviscid results. We computed the absolute instability range of the inviscid Rayleigh equation as shown in Figure 10 (a), which is the same as the one displayed in [23]. In the β interval shown in the figure, the complex α, complex ω and the wave-angle ε parameters which constitute the absolutely unstable regime of the inviscid-flow over a rotating-disk boundary layer are identified. In compliance with the findings of [23], it is

seen from the figure that for long wavelengths, near the vicinity of the origin, the flow is neutrally absolutely unstable.

The range of absolute instability which is given by the positive sign of ω_i ceases near the azimuthal wave-number $\beta = 0.265$. Here, the corresponding eigenvalues are ω_r = -0.070, $\alpha = 0.34$ - i 0.058 and $\varepsilon = 38.12^o$, respectively. These points are the upper limits of the region of absolute instability.

Brigg's criterion as described earlier requires a branch point singularity between two or more spatial branches of the dispersion relation, of which, at least two must lie in the distinct halves of the complex α plane when ω_i is sufficiently large and positive. To demonstrate this feature, we have plotted the two spatial branches in Figure 11 for which the branches merge in the distinct half-α planes, for sufficiently large positive values of $\mathrm{Im}(\omega) =$ constant, when ω traces a horizontal line in the ω plane. Figure 11 (b) shows the progression of the two spatial branches in the α plane at $\beta = 0.1$. The corresponding ω_i's to each figure are 0.045, 0.021, 0.012 (pinching point) and 0.011, respectively. As $\mathrm{Im}(\omega)$ is lowered down towards 0.012 from the large values of $\mathrm{Im}(\omega)$, there occurs a pinching-point in the ω plane at $\omega = \omega_p = -0.023 + i0.012$, and a corresponding saddle-point in the α plane at $\alpha = \alpha_s = 0.24 - i0.0680$ as shown in the third part of the figure. Since the sign of ω_i is positive, this point gives an absolute growth rate in the flow. The last portion of the graph shows branch interchanging after pinching has taken place.

7.2. Viscous results. The viscous absolute instability boundaries were calculated in [23] and [15]. The pinching phenomenon is shown in Figure 11 (a) for $R = 524$ and $\beta = 0.1$. At large positive values of ω_i, the branches shown lie in distinct halves of the α plane. At the pinching point, ω_i is 0.15, and so this point exhibits absolute instability. The branches drawn in the figure are for $\omega_i = 5.34$, 2.15, 0.15, and 0, respectively. The corresponding wave-number α is $0.20 - i0.112$, and the wave-angle $\varepsilon = 26.6^o$. Note that the qualitative behavior of the spatial branches is very similar to that for the inviscid case in Figure 11 (b).

Figure 11 (b) shows the parameter regions of neutral absolute instability in the (R, β), (R, ω_r), (R, α_r), (R, α_i) and (R, ε) planes. Inside the curves the imaginary part of the frequency ω is positive and thus the particular flow there is absolutely unstable. Outside, the flow becomes convectively unstable. The critical Reynolds number for the flow to undergo absolute instability was found to be $R = 507.40$, and the corresponding eigenvalues are $\beta = 0.135$, $\alpha = (0.217, -0.122)$, $\omega = -17.72$ and $\varepsilon = 31.84^o$, respectively. Note that Lingwood (1995) calculated the critical Reynolds number of absolute instability as 510 and later corrected this value in [24] to 507.30, which is very close to the value obtained here. We believe that the discrepancy between these two results is due to the different numerical methods employed. Experiments reveal that transition occurs at approximately $R = 513$. Below this critical value, ω_i can be reduced to zero in the calculation of the integral given in (27), before the occurrence of pinching, indicating that the flow is only convectively unstable. As Healey [18] recently demonstrated from his asymptotic theory of the upper branch neutral modes, the pinch-point displayed in Figure 11 (b) does not asymptote towards the inviscid neutral curve of Figure 10 (a). Healey [18] concludes that the branch points of Figure 10 (a) rather have a viscous long-wave origin.

To make a comparison with the inviscid absolutely unstable region of Figure 10 (a) and its viscous origin, we have obtained the solutions at a sufficiently large Reynolds number, namely $R = 15000$. The viscous equations in this case result in an absolutely unstable region as shown in Figure 12 (a). The upper limit in both cases is almost identical, yielding a value of azimuthal wave-number $\beta = 0.265$. In Figure 12 (b) the behavior of

the eigenfunction of the normal velocity component (h) is shown again at $R = 15000$. The significance of the results displayed in Figure 12 is due to its demonstration that the inviscid branch points have a viscous correspondence.

8. Direct spatial resonance results

The Benney [3] resonance mechanism with modal coalescence can also be observed for three dimensional disturbances. In fact, the existence of several modes in the rotating-disk flow, of which at least two have opposite wave energies (family 1 and family 2) signifies modal coalescence. As mentioned in the introduction, when two coalescing modes originate from waves propagating in the same direction as in the case of a convectively unstable flow, then the corresponding branch point is not a pinch-point, but only a double-pole of the dispersion relation. According to linear theory, such disturbances normally will decay ultimately. However, the short-term algebraic growth associated with such a double-pole may be decisive and the corresponding potentially large amplitudes may initiate nonlinearity and so carry the whole system into the nonlinear stages. This may be particularly important provided that the coalescing modes are linearly neutral. Consequently, the corresponding local response to the damping rates given as $\mathrm{O}(\frac{1}{\alpha_i})$ can be so large that it may initiate the nonlinear stages before the exponentially growing modes, which is implied by the recent numerical simulation results of [10, 11]). Such resonance cases between coalescing modes occurring in the same α plane has been studied by [21]. He investigated the direct resonance in a plane Poiseuille flow and in a Blasius boundary layer flow, which are typical examples of convectively unstable flows.

Figure 13 (b) shows such neutral branch point curves, as a function of Reynolds number. It can be seen in the fourth figure that in the vicinity of a Reynolds number of 445 there occurs direct resonance, in fact it starts at this Reynolds number, where α_i becomes almost zero. In order to support this, in Figure 13 (a) we plot two spatial branches both emerging in the upper half α plane. Here, the particular set of parameters are $\beta = 0.0387$, $\alpha = (0.184, 0.0)$ and $\omega = (3.25{,}0)$, respectively. This point is clearly a bifurcation point with a real ω from which several branches emerge. An indication of the achievable amplitude amplification at this resonance point can be evaluated as the inverse of α_i, for which α_i is practically zero. Therefore it is suggested that, unlike plane Poiseuille flow or Blasius boundary layer flow, direct resonance could be physically relevant in the rotating-disk boundary layer flow. At this Reynolds number of 445 the flow is still in the laminar region. It should also be mentioned that we did not encounter any other branch point apart from the above point which seems to be the only point leading to direct spatial resonance.

9. Conclusions

The linear stability features of the rotating-disk boundary layer flow have been re-examined. The stability parameters of the stationary as well as non-stationary waves have been computed and stability diagrams have been produced using a Spectral method based on a Chebyshev collocation approximation as well as a fourth-order Runge-Kutta integration technique. The results obtained within this study are totally in line with the previously found results cited in the references herein. The findings are briefly summarized below.

9.1. Convective instability. It has been found that for positive frequencies there exists two minimum points on the neutral stability curves. One of these is related to the inviscid-type instability occurring on the upper branch and the other one is located on the lower branch associated with the viscous-type instability. For increasing positive

frequencies, the lower-branch curve is more discernible. The lowest critical Reynolds number on this branch was found to be 64.443 and it occurs at the frequency $\omega = 7.9$. The lowest critical Reynolds number on the upper-branch however, occurs at a negative frequency.

The upper-branch neutral stability of three dimensional disturbances imposed on the Von Kármán's boundary layer profile has been investigated asymptotically in particular for the non-stationary cross-flow disturbances. It has been found that at very large Reynolds numbers, the upper branch for all waves tends asymptotically to a finite value. The asymptotic analysis of [17] has been extended to include the non-zero frequency waves for the upper branch instability modes. Travelling waves with negative frequencies as well as positive frequencies approach one branch of the zero-frequency neutral curve corresponding to an angle of about 10.6°. The growth rate for a wave with negative wave-angle has been found to be small compared with that for the waves with positive wave-angle.

9.2. Absolute instability. We have also investigated the absolute stability characteristics of the three dimensional boundary-layer flow due to a rotating-disk. The singularities in the dispersion relation have been studied and several results have been obtained. First, the coalescing modes of spatial and temporal instability waves originate from waves propagating in opposite directions. This type of branch point singularity is known to be related to the absolute instability in a specific range of the parameter space. Therefore, we can conclude that, above a certain critical Reynolds number, which has been found to be 507.40 in this study, the flow over the rotating-disk becomes absolutely unstable, causing the disturbances at a fixed radial point in space to grow to large amplitudes in time. Otherwise, below the critical point the flow is convectively unstable, showing that growing disturbances travel downstream and eventually leave the flow undisturbed.

The second main result from this work is that, the coalescing modes which originate in the same α wave-number plane form a second-order singularity. This kind of singularity has been found to occur in the laminar regime of the flow at about $R = 445$. The existence of such singularities which lead to the direct spatial resonance of the modes may cause a locally algebraic growth and consequently the initiation of nonlinearity.

Finally the work presented here may be extended in many ways. For example, one could compare the neutral stability and growth rates for both the stationary and non-stationary cross-flow vortices with the asymptotic theory of [14] in the case of high Reynolds numbers ($R >> 1$). As we have mentioned before, the analysis presented here is a local analysis in which the non-parallel effects were omitted. How non-parallelism will affect the absolute instability regime determined from this investigation requires further work and moreover requires the numerical treatment of the full linearized stability equations outlined in this report. Therefore, a more global analysis which makes use of non-parallel effects should also be considered.

Figure 1. Von-Karman's Velocity Distribution in the Rotating-disk Flow

(a) Von-Karman's self-similarity solutions corresponding to the basic field of the rotating-disk flow; cross-flow velocity (F), azimuthal velocity (G) and normal velocity to the disk (H),

(b) Shapes of the combined velocity ($\alpha F + \beta G$) for selected Reynolds numbers. Left: Stationary ($\omega = 0$) cross-flow velocity profiles starting from the upper branch; (..) $R = 15000$ and (–) $R = 286.045$, to the lower branch; (--) $R = 453.755$ and (– –) $R = 15000$. Right: Non-stationary profiles of $\omega = 7.9$ for the same conditions,

(c) Neutral stability curves in the (R, α) plane, and

(d) In the (R, ε) plane; (..) $\omega = -5$, (--) $\omega = 0$, (– –) $\omega = 4$, (—) $\omega = 7.9$ and (— —) $\omega = 10$.

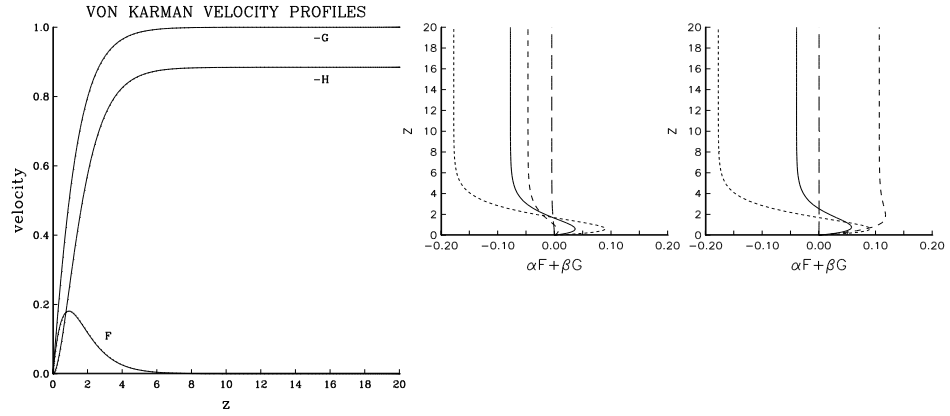

(a) (b)

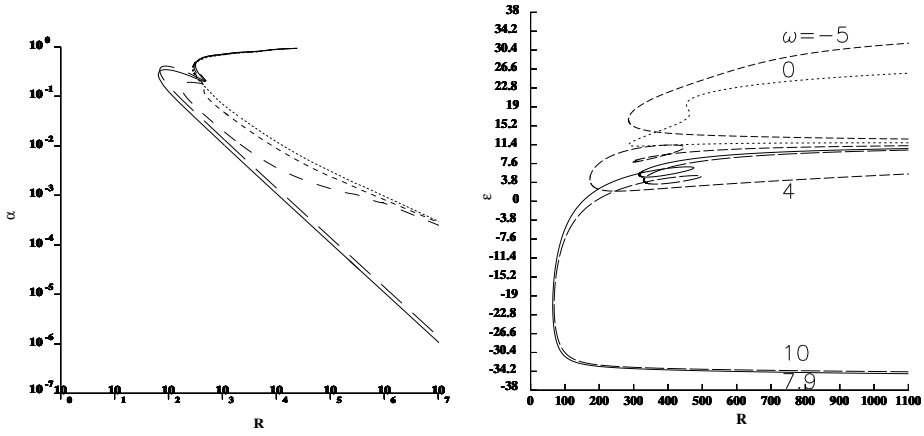

(c) (d)

Figure 2. Stability Curves in the (R, α), (R, β) and (R, ε) Planes for $\omega = 0$ and $\omega = 4$ Waves

(a-c): Stability curves for $\omega = 0$ waves,

(d-f): Stability curves for $\omega = 4$ waves.

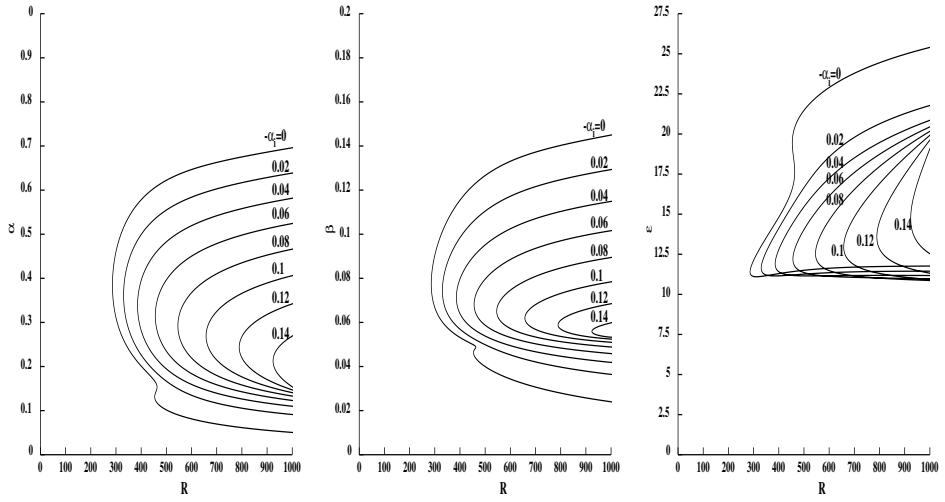

(a) (b) (c)

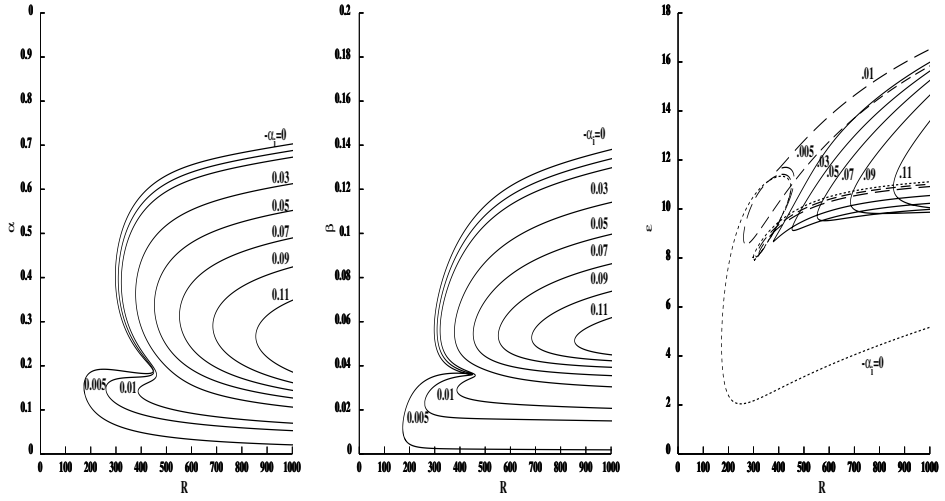

(d) (e) (f)

Figure 3. Growth Rate Curves for Zero-frequency and Frequency-10 Waves

(a-b) Distribution of the spatial amplification rate of zero-frequency, family 1 normal modes as a function of wave-angle at a Reynolds number of 1000 for zero and frequency 10 modes, respectively,

(c-d) Maximum spatial amplification rate $-\alpha_i$, radial wave-number α_r, azimuthal wave-number β and wave-angle ε are shown against frequency at a Reynolds number of 500.

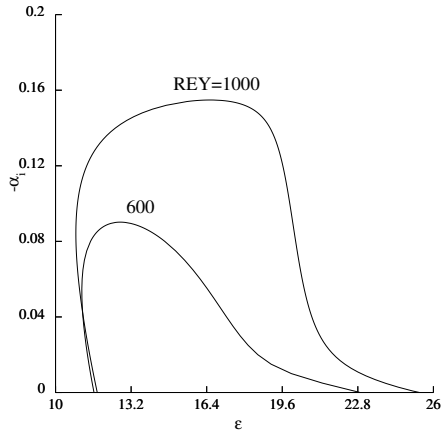

(a)

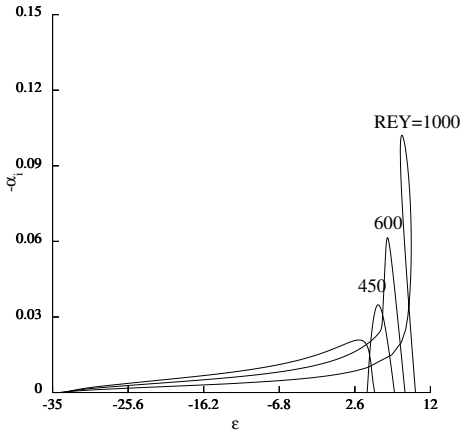

(b)

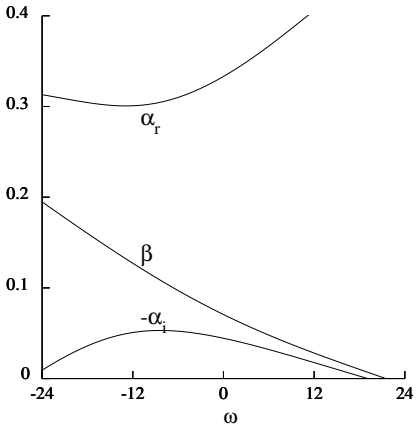

(c)

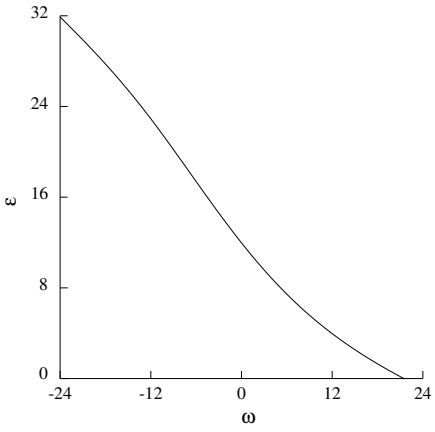

(d)

Figure 4. Spatial Branches of Zero-Frequency Waves at $R = 400$, 1000 and 15000

Emerging branches of three families of stationary waves at $R = 400$ for:
(a-c) Zero frequency waves,
(d-f) 7.9 frequency waves.

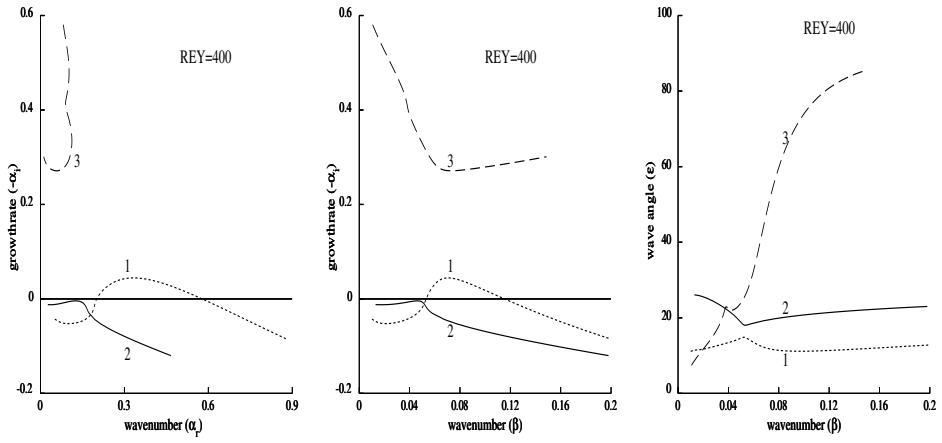

(a) (b) (c)

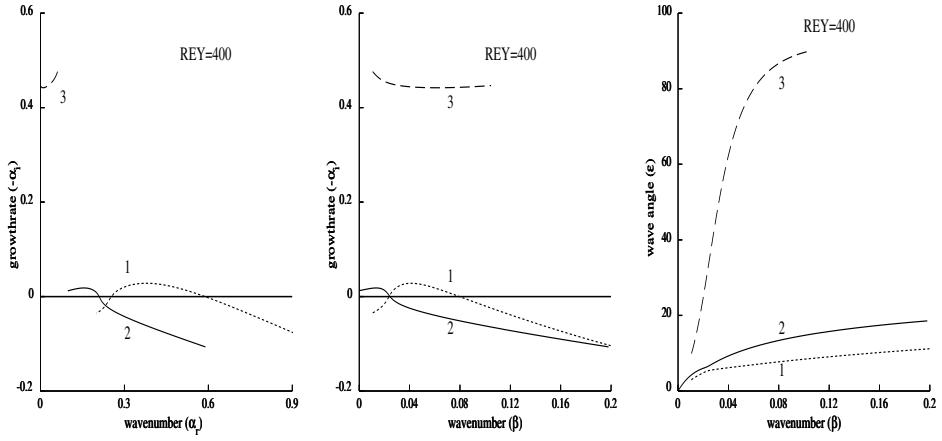

(d) (e) (f)

Figure 5. Isosurfaces for $\omega = 0$ Waves

(a-b) Contour-lines for $\omega = 0$ at the critical eigenvalues $R = 286.045$, $\alpha = 0.38407$, $\beta = 0.07745$, and

(c-d) Contour-lines for $\omega = 7.9$ at the critical eigenvalues $R = 316.601$, $\alpha = 0.42108$, $\beta = 0.03933$.

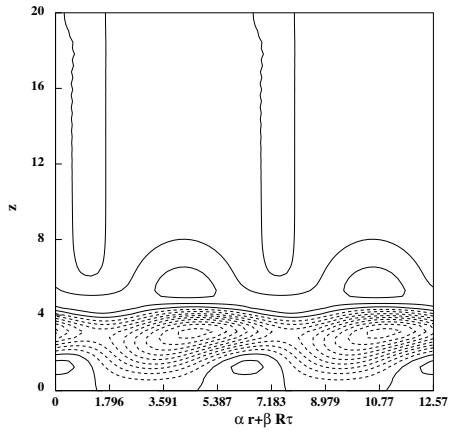

(a)

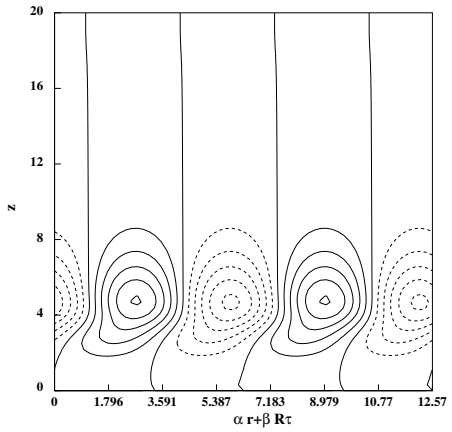

(b)

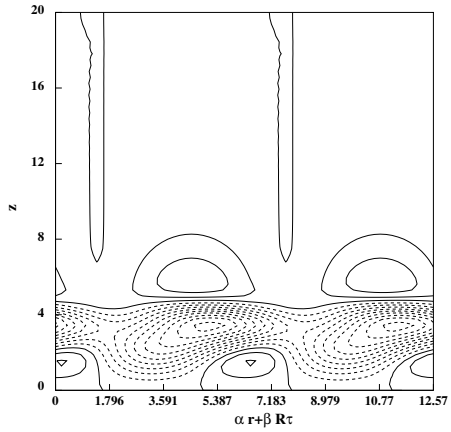

(c)

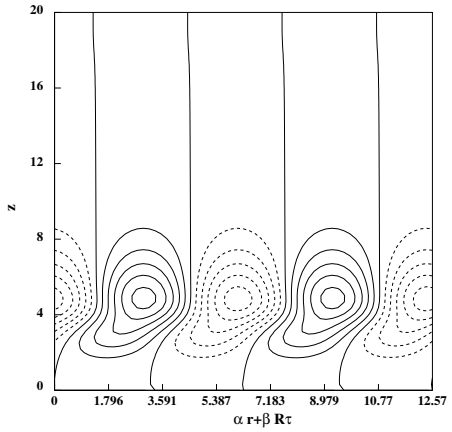

(d)

Figure 6. Stationary Cross-flow Vortices in the Rotating Boundary Layer Flow

(a-b) Stationary cross-flow vortex structure is at the critical eigenvalues (a) $R = 286.045$, $\alpha = 0.38407$, $\beta = 0.07745$; (b) $R = 453.755$, and

(c-d) Travelling cross-flow vortex structure ($\omega = 7.9$) is at the critical eigenvalues (c) $R = 316.601$, $\alpha = 0.42108$, $\beta = 0.03933$, (d) $R = 64.443$, $\alpha = 0.27597$, $\beta = -0.10669$.

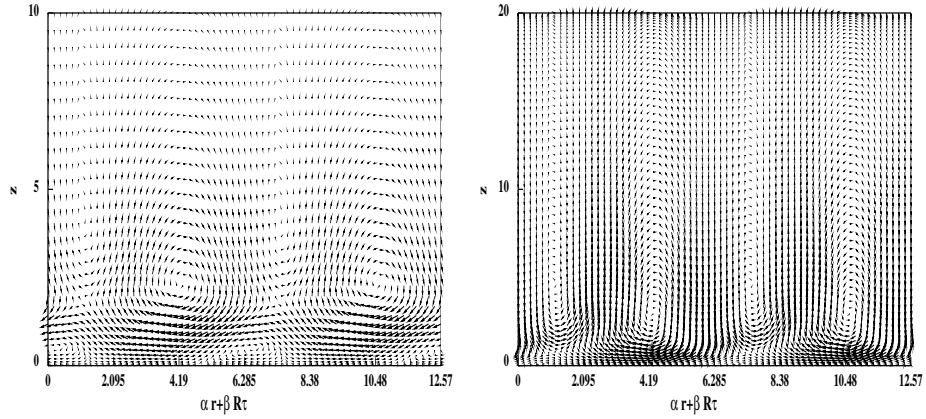

(a) (b)

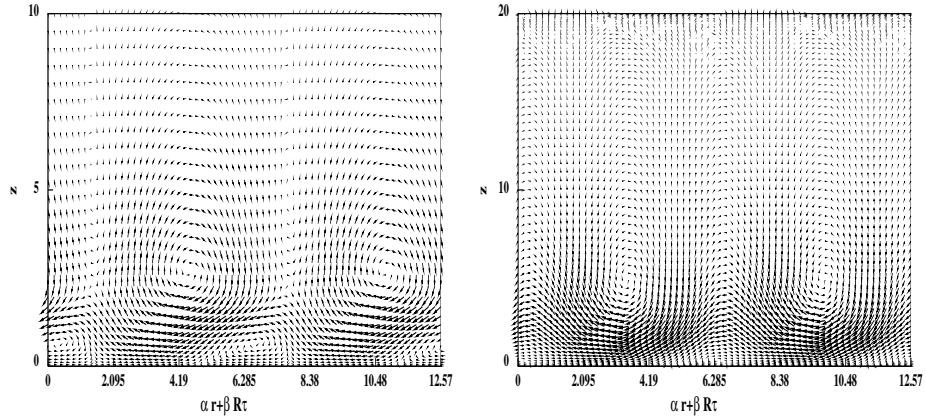

(c) (d)

Figure 7. Upper Branch Modes from Asymptotic Approach

A comparison of the numerical and asymptotic calculations of the stationary – and non-stationary -- ($\omega = -5$) and $--$ $\omega = 10$ waves, in the (R, λ) and (R, ε) planes. In the figures the long curves show numerical results and the shorter lines asymptotic ones.

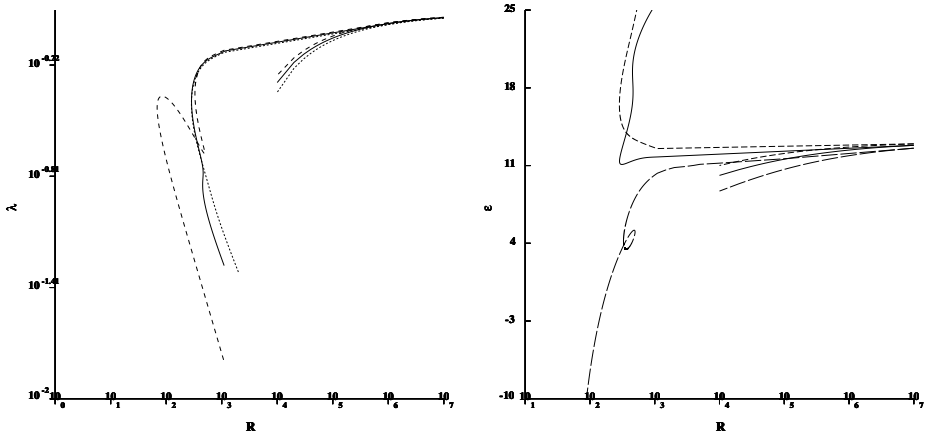

(a) (b)

Figure 8. Absolute Instability Range in the Mixing Layer

Absolutely and convectively unstable range and branch points in the mixing layer problem are demonstrated.

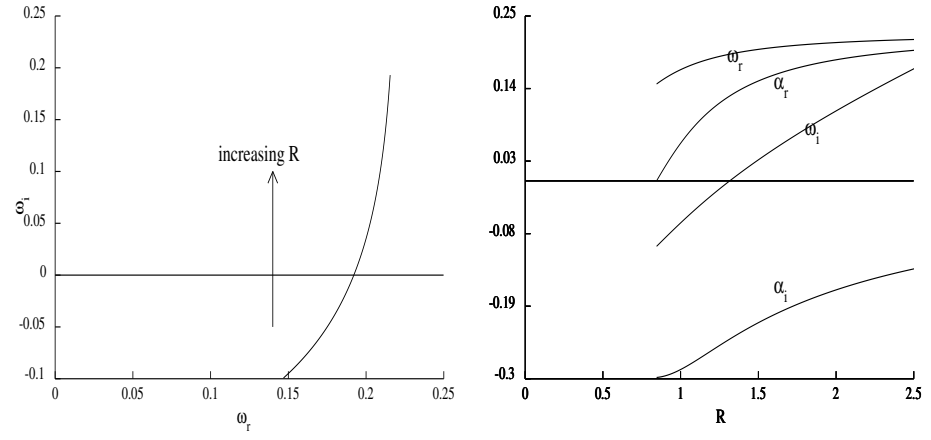

(a) (b)

Figure 9. A Sketch of the Instability Branches and the Impulse Response

Sketches of the typical temporal (a), (c), (e) and spatial (b), (d), (f) branches are demonstrated. The physical impulse response is shown corresponding to

(g) convectively unstable flow, and

(h) absolutely unstable flow.

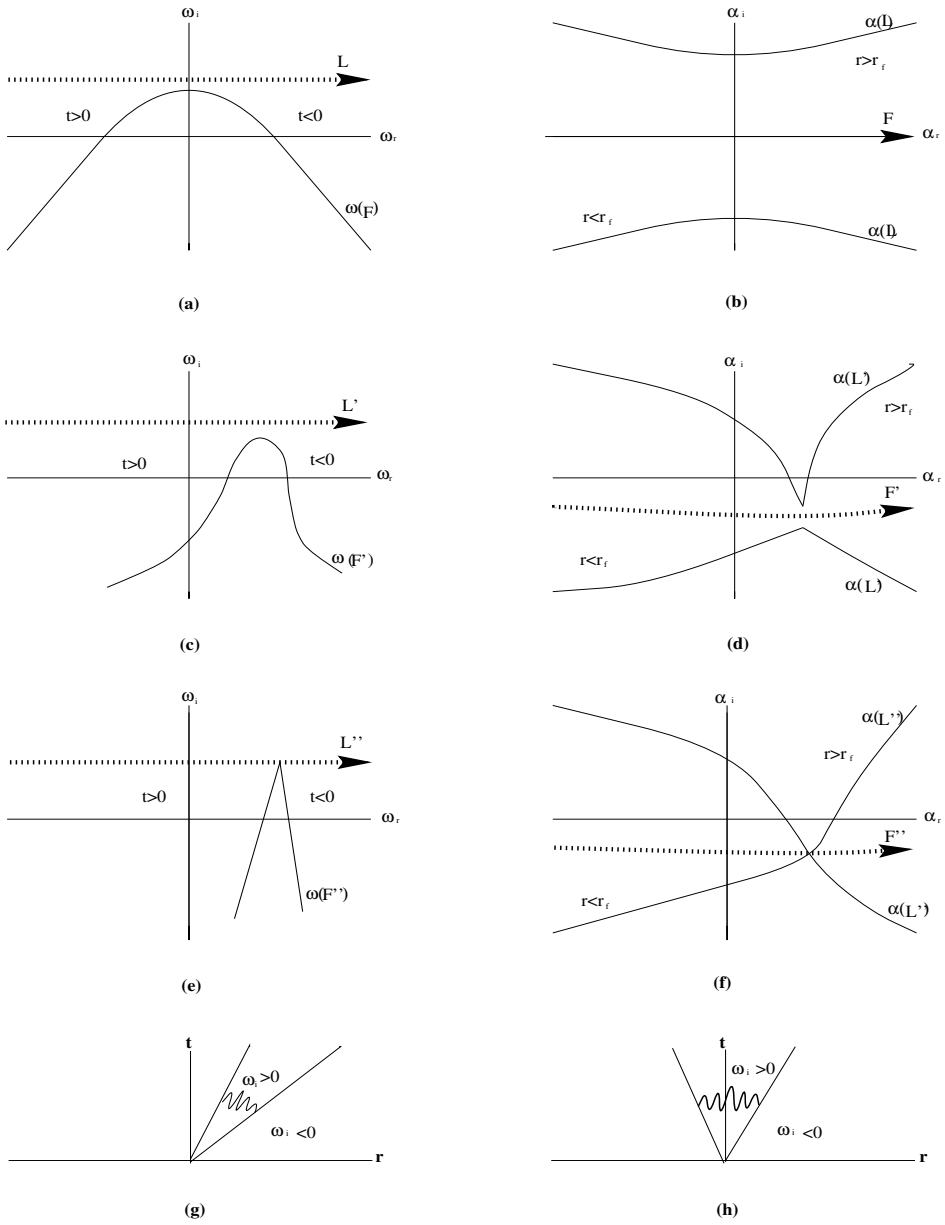

Figure 10. Absolute Instability Range and Pinching Phenomenon in the Inviscid Rotating-disk Flow.

(a) Plot showing the locus of the branch-points (ω, α) against β. Variation of wave-angle ε is also given. Data is taken from the solution of the inviscid Rayleigh equation (7) and clarifies the range where the rotating-disk flow becomes inviscidly absolutely unstable,

(b) Demonstrating the progression of the two spatial branches in the α plane at $\beta = 0.1$ as ω traces a horizontal line, in the inviscid rotating-disk flow. Figures are respectively for $\omega_i = 0.045$, $\omega_i = 0.021$, $\omega_i = 0.012$ (pinching point), $\omega_i = 0.011$. Pinching takes place in the third portion and clearly demonstrates a true pinching in the sense that Briggs-Bers criterion is satisfied. The direction of the arrows indicates increasing frequency.

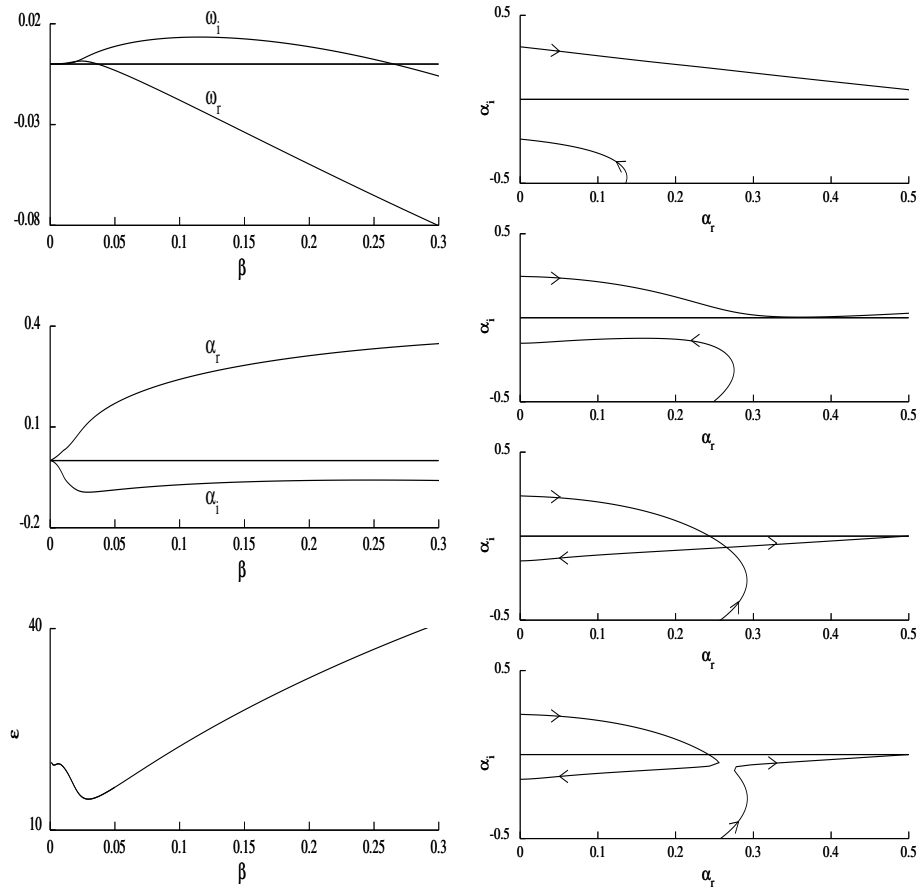

(a) (b)

Figure 11. Pinching Phenomenon and Neutral Absolute Instability Curves in the Viscous Rotating-disk Flow

(a) Pinching phenomena in the viscous rotating-disk boundary layer flow. Branch point at $\beta = 0.1$, $\alpha = (0.20, -0.112)$, $\omega = (16.69, 0.15)$ and $R = 524$ (third portion). Graphs are for $\omega_i = 5.34$, 2.15, 0.15, 0, respectively. Pinching requirements are satisfied. The direction of the arrows indicates increasing frequency,

(b) Neutral absolute instability curves defining the region of absolute instability in the viscous rotating-disk boundary-layer flow are shown in the (R, β), (R, ω_r), (R, α_r), (R, α_i) and (R, ε) planes, respectively. For all the curves, inside the loop signifies absolute instability, while outside we have convective stability/instability.

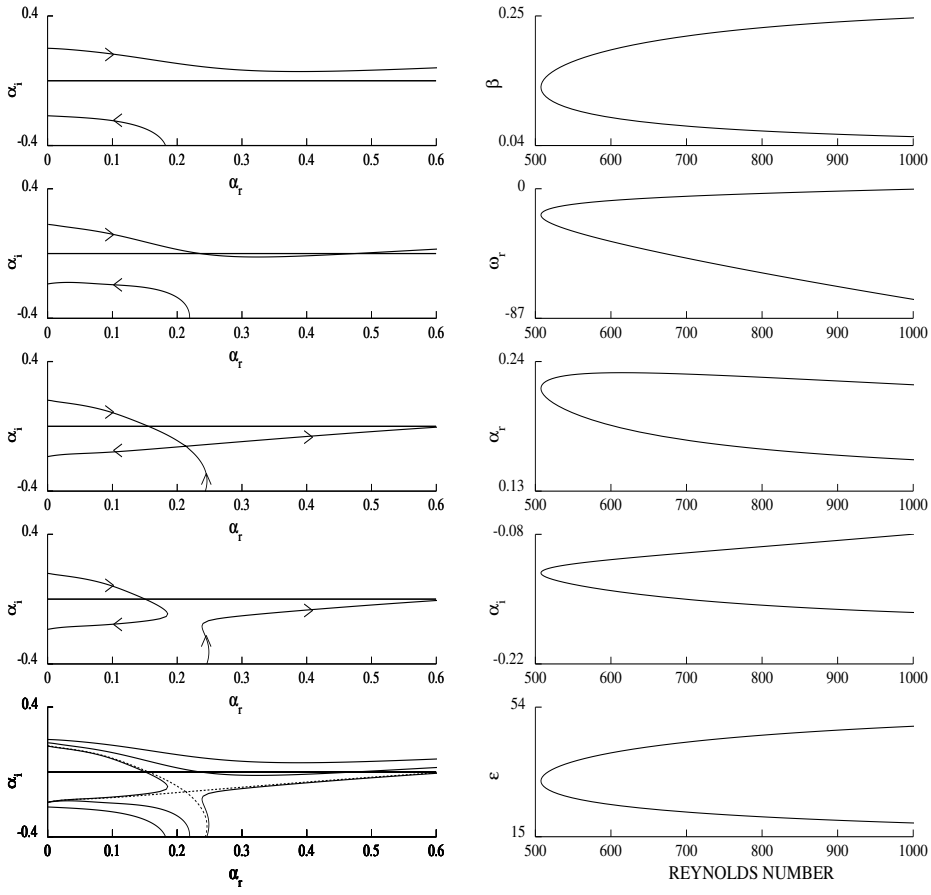

(a) (b)

Figure 12. Absolute Instability Range and Eigenfunction h at $R = 15000$

(a) Locus of the branch points (ω, α) are given as β varies. Variation in ε is also given. Data is taken from the solution of the full sixth-order viscous equations (6) for $R = 15000$ and reveals the range where the rotating-disk flow becomes viscously absolutely unstable,

(b) Eigenfunctions of the normal velocity component (h) are shown in the viscous rotating-disk boundary flow layer at $R = 15000$.

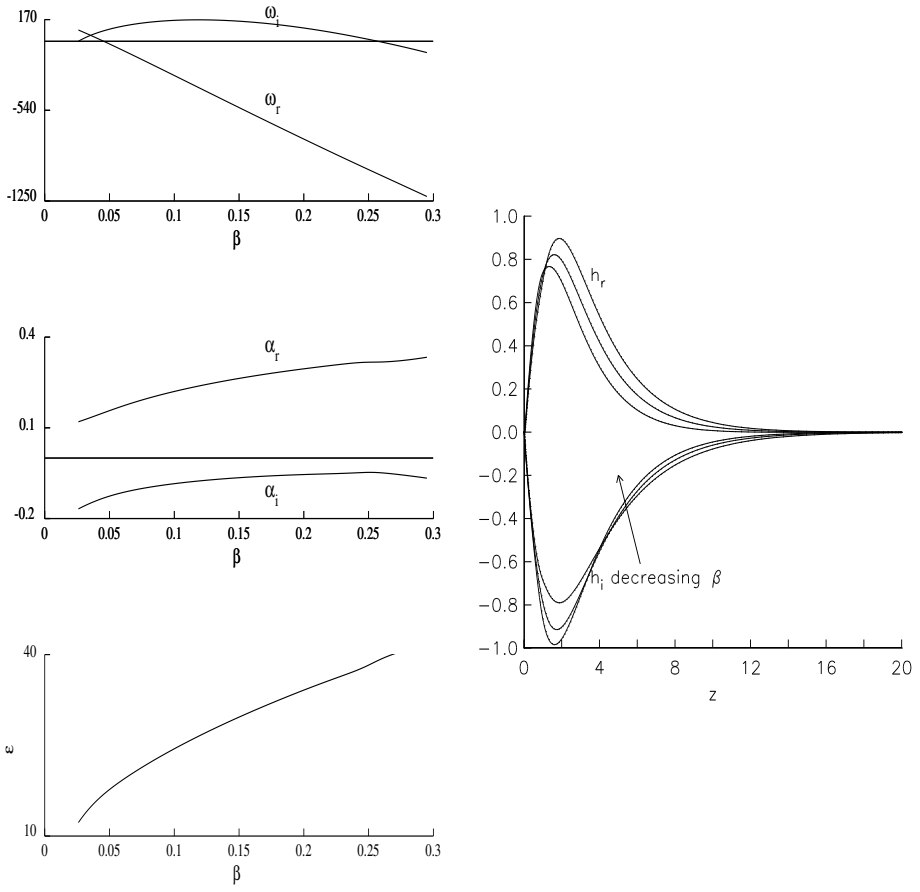

(a) (b)

Figure 13. Pinching Phenomena and Neutral Branch Points in the Viscous Rotating-disk Flow

(a) The progression of the two spatial branches at $R = 445$ and $\beta = 0.0387$, in the α plane is given in the viscous rotating-disk boundary layer flow. Graphs are for $\omega_i = 5, 2, 0.25, 0$ and -0.02, respectively. Branch point is at α = (0.184,0), ω = (3.25,0) (fourth portion). A direct spatial resonance occurs between the two spatial branches since the corresponding α and ω are neutral. The direction of the arrows indicates increasing frequency,

(b) Neutral branch points of two merging branches from the same α plane are shown.

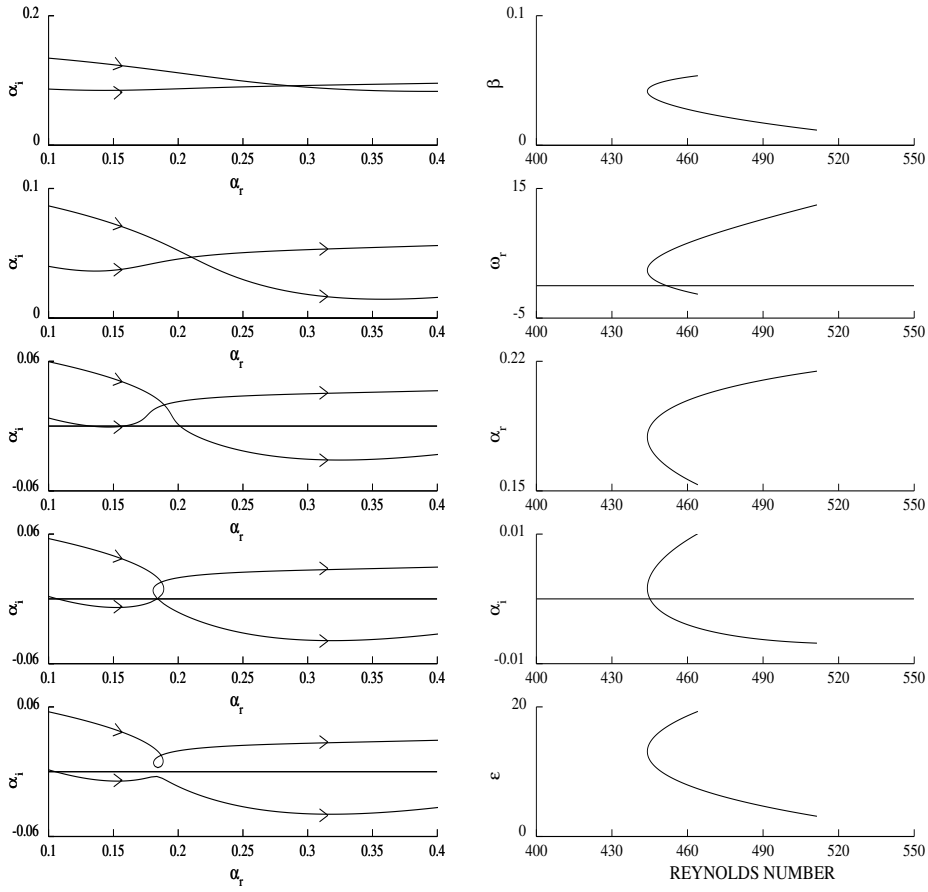

(a) (b)

Appendix A

The quantities arising from the upper branch asymptotic analysis in §1.5.5. are:

$$k_c = \left[\beta_0 r\hat{e}\frac{1}{\bar{U}'_B}\frac{[}{F}^{''} - F\bar{U}'''_B\bar{U}'_B] + \omega_0\frac{\bar{U}''''_B}{\bar{U}'^2_B}\right]_{\zeta=\bar{\zeta}}.$$

$$I_1 = \int_0^\infty w_0^2 d\zeta,$$

$$I_2 = \beta_0\int_0^\infty \frac{1}{\bar{U}_B}[F'' - F\frac{\bar{U}''_B}{\bar{U}_B}]w_0^2 d\zeta,$$

$$I_3 = \int_0^\infty \frac{\bar{U}''_B}{\bar{U}^2_B} w_0^2 d\zeta,$$

$$a = i\pi\beta_0 w_0^2(\bar{\zeta})\mathrm{sgn}[\bar{U}'_B(\bar{\zeta})]\left[\frac{1}{|\bar{U}'_B|}[F'' - F\frac{\bar{U}'''_B}{\bar{U}'_B}]\right]_{\zeta=\bar{\zeta}},$$

$$b = i\pi w_0^2(\bar{\zeta})\mathrm{sgn}[\bar{U}'_B(\bar{\zeta})]\left[\frac{1}{\bar{U}'_B}\frac{1}{|\bar{U}'_B|}\bar{U}'''_B\right]_{\zeta=\bar{\zeta}}.$$

References

[1] Balakumar, P. and Malik, M. R. *Travelling disturbances in rotating-disk flow*, Theoret. Comput. Fluid Dyn. **2**, 125–137, 1990.

[2] Bassom, A. P. and Gajjar, J. S. B. *Non-stationary cross-flow vortices in a three-dimensional boundary layer*, Proc. Roy. Soc. London Ser. A **417**, 179–212, 1988.

[3] Benney, D. J. and Gustavsson, L. H. *A new mechanism for linear and non-linear hydrodynamic instability*, Stud. Appl. Math. **64**, 185–209, 1981.

[4] Bers, A. *Linear waves and instabilities*, Physique des Plasmas., 117–225, 1975.

[5] Betchov, R. and Criminale, W. O. *Spatial instability of the inviscid jet and wake*, Phys. Fluids. **9**, 359–362, 1966.

[6] Briggs, R. J. *Electron-Stream Interaction With Plasmas* (MIT Press, 1964).

[7] Cole, J. W. *Hdrodynamic stability of compressible flows*, PhD thesis (University of Exeter, 1995).

[8] Cooper, A. J. and Carpenter, P. W. *The stability of rotating-disk boundary-layer flow over a compliant wall. part i. type i and ii instabilities*, J. Fluid Mech. **350**, 231–259, 1997.

[9] Cooper, A. J. and Carpenter, P. W. *The stability of rotating-disk boundary-layer flow over a compliant wall. part ii. absolute instability*, J. Fluid Mech. **350**, 261–270, 1997.

[10] Davies, C. and Carpenter, P. W. *A novel velocity-vorticity formulation of the navier-stokes equations with application to boundary layer disturbance evolution*, J. Comput. Phys. **172**, 119–165, 2001.

[11] Davies, C. and Carpenter, P. W. *Global behaviour corresponding to the absolute instability of the rotating-disc boundary layer*, J. Fluid Mech. **486**, 287–329, 2003.

[12] Faller, A. J. and Kaylor, R. E. *A numerical study of the instability of the laminar ekman boundary layer*, J. Atm. Sci. **23**, 466–480, 1966.

[13] Federov, B. I., Plavnik, G. Z., Prokhorov, I. V. and Zhukhovitskii, L. G. *Transitional flow conditions on a rotating-disk*, J. Eng. Phys. **31**, 1448–1453, 1976.

[14] Gajjar, J. S. B. *Nonlinear evolution of a 1st mode oblique wave in a compressible boundary-layer. Part 1. Heated cooled walls*, IMA Journal of Applied Mathematics **53**, 221–248, 1994.

[15] Jasmine, H. A. and Gajjar, J. S. B. *Convective and absolute instability in the incompressible boundary layer on a rotating disk in the presence of a uniform magnetic field*, Journal of Engineering Mathematics **52**, 337–353, 2005.

[16] Gregory, N., Stuart, J. T. and Walker, W. S. *On the stability of three-dimensional boundary layers with applications to the flow due to a rotating-disk*, Philos. Trans. R. Soc. London Ser. A **248**, 155–199, 1955.

[17] Hall, P. *An asymptotic investigation of the stationary modes of instability of the boundary layer on a rotating-disk*, Proc. Roy. Soc. London Ser. A **406**, 93–106, 1986.

[18] Healey, J. J. *On the relation between inviscid and viscous absolute instability of the rotating-disk boundary layer*, J. Fluid Mech. **511**, 179–199, 2004.
[19] Huerre, P. and Monkewitz, P. A. *Absolute and convective instabilities in free shear layers*, J. Fluid Mech. **159**, 151–168, 1985.
[20] Huerre, P. and Monkewitz, P. A. *Local and global instabilities in spatially developing flows*, Ann. Rev. Fluid Mech. **22**, 473–537, 1990.
[21] Koch, W. *Direct resonance in orr-sommerfeld equation*, Acta Mech. **58**, 11–29, 1986.
[22] Kupfer, K., Bers, A. and Ram, A. K. *The cusp map in the complex-frequency plane for absolute instabilities*, Phys. Fluids. **30**, 3075–3082, 1987.
[23] Lingwood, R. J. *Absolute instability of the boundary layer on a rotating-disk*, J. Fluid Mech. **299**, 17–33, 1995.
[24] Lingwood, R. J. *On the application of the briggs' and steepest-descent method to a boundary-layer flow*, Stud. Appl. Math. **98**, 213–254, 1997.
[25] Mackerrel, S. O. *A nonlinear asymptotic investigation of the stationary modes of instability of the 3-dimensional boundary layer on a rotating-disk*, Proc. Roy. Soc. London Ser. A **413**, 497–513, 1987.
[26] Malik, M. R. *The neutral curve for stationary disturbances in rotating-disk flow*, J. Fluid Mech. **164**, 275–287, 1986.
[27] Malik, M. R. and Poll, D. I. A. *Effect of curvature on three-dimensional boundary layer stability*, AIAA Journal **23**, 1362–1369, 1985.
[28] Malik, M. R., Zang, T. A. and Hussaini, M. Y. *A spectral collocation method for the navier-stokes equations*, J. Comput. Phys. **61**, 64–88, 1984.
[29] Monkewitz, P. A. *The absolute and convective nature of instability in two-dimensional wakes at low reynolds numbers*, Phys. Fluids. **31**, 999–1006, 1988.
[30] Pier, B. *Finite-amplitude crossflow vortices, secondary instability and transition in the rotating-disk boundary layer*, J. Fluid Mech. **487**, 315–343, 2003.
[31] Shanthini, R. *Degeneracies of the temporal orr-sommerfeld eigenmodes in plane poiseuille flow*, J. Fluid Mech. **201**, 13–34, 1989.
[32] Turkyilmazoglu, M. and Gajjar, J. S. B. *On the absolute instability of the attachment-line and swept-hiemenz boundary layers*, Theoret. Comput. Fluid Dyn. **13**, 57–75, 1999.
[33] Turkyilmazoglu, M., Gajjar, J. S. B. and Ruban, A. I. *The absolute instability of thin wakes in an incompressible/compressible fluid*, Theoret. Comput. Fluid Dyn. **13**, 91–114, 1999.
[34] Wilkinson, S. P. and Malik, M. R. *Stability experiments in the flow over a rotating-disk*, AIAA Journal **23**, 588–595, 1985.